Sensitivity of liquid cloud optical thickness and effective radius retrievals to cloud bow and glory conditions using two SEVIRI imagers

Nikos Benas[1], Jan Fokke Meirink[1], Martin Stengel[2], Piet Stammes[1]

5   [1]Royal Netherlands Meteorological Institute (KNMI), De Bilt, The Netherlands
[2]Deutscher Wetterdienst (DWD), Offenbach, Germany

Correspondence to: Nikos Benas (benas@knmi.nl)

Abstract. Retrievals of cloud properties from geostationary satellite sensors offer extensive spatial and temporal coverage and resolution. The high temporal resolution allows the detection of diurnally resolved cloud properties. However, retrievals

10   are sensitive to varying illumination and viewing geometries, including cloud glory and cloud bow conditions, which can lead to irregularities in the diurnal data record. In this study, these conditions and their effects on liquid cloud optical thickness and effective radius retrievals were analyzed using the Cloud Physical Properties (CPP) algorithm. This analysis was based on the use of SEVIRI reflectances and products from Meteosat-8 and -10, which are located over the Indian and Atlantic Ocean, respectively, and cover an extensive common area under different viewing angles. Comparisons of the

15   retrievals over different underlying surfaces (ocean/land) and using different spectral combinations of visible and shortwave-infrared channels were also performed, to assess the importance of these factors in the retrieval process. The sensitivity of the cloud bow and glory related irregularities to the width of the assumed droplet size distribution was analyzed by using different values of the effective variance of the size distribution. The results suggest for marine stratocumulus clouds an effective variance of around 0.05, which implies a narrower size distribution than typically assumed in satellite-based

20   retrievals. For a case with continental clouds a broader size distribution (effective variance around 0.15) was obtained. This highlights the importance of appropriate size distribution assumptions and provides a way to improve the quality of cloud products in future climate data record releases.

1 Introduction

Low warm clouds contribute a large part of the overall cloud effects and feedbacks on the climate system (Zhou et al., 2016).

25   Forming uniform decks, especially over large oceanic areas around the globe, they increase the planetary albedo and exert a cooling effect in the Earth's radiative balance (Wood, 2012).

Optical and microphysical properties of liquid clouds, specifically optical thickness (τ) and effective radius (r_e), are important for the estimation of cloud-radiation interactions and the consequent effects on the atmospheric radiation budget.

They are also used for the calculation of the cloud droplet number concentration (CDNC), which is a key parameter for the assessment of aerosol-cloud interactions (Grosvenor et al., 2018), and the cloud liquid water path (LWP), which is a crucial component of the water cycle (Wood and Hartmann, 2005). Furthermore, climate models rely on the measurements or retrieval of these cloud properties for the evaluation of their relevant parameterizations (e.g. Pincus et al., 2012).

These characteristics highlight the importance of continuous monitoring of clouds and their properties, which on a global scale is possible only through satellite observations. In fact, during the last decades, substantial advances have been made regarding the continuous and reliable retrieval of cloud properties. Cloud property data records derived from satellite-based passive visible-infrared (VIS-IR) imagers start already in the early 1980s, based on Advanced Very High Resolution

10 Radiometer (AVHRR) measurements from polar orbiting satellites, e.g. the Satellite Application Facility on Climate Monitoring (CM SAF) Cloud, Albedo and Surface Radiation dataset from AVHRR data - second edition (CLARA-A2, Karlsson et al., 2017) and the Pathfinder Atmospheres - Extended (PATMOS-x, Heidinger et al., 2014) data records; combinations of measurements from polar orbiting sensors, e.g. the Cloud_cci data records, which are based on AVHRR, MODIS, ATSR-2 and AATSR (Stengel et al., 2017); and measurements from polar and geostationary satellites, e.g. the

15 International Satellite Cloud Climatology Project (ISCCP) data set (Young et al., 2018). Additionally, more recent and advanced sensors provide high spatial and temporal resolution in more spectral channels, also increasing the number and reliability of cloud properties retrieved. Examples of such sensors include the Moderate Resolution Imaging Spectroradiometer (MODIS) and the homonymous cloud data set (Platnick et al., 2017), and the Spinning Enhanced Visible and Infrared Imager (SEVIRI) and the corresponding Cloud property dAtAset using SEVIRI - second edition (CLAAS-2)

20 data record (Benas et al., 2017).

Cloud optical and microphysical properties are presently routinely retrieved from passive VIS-IR satellite imager measurements, basically following the "Nakajima-King" approach (Nakajima and King, 1990). This retrieval principle is based on the combination of a visible/near-infrared channel in which clouds are non-absorbing and the reflectance is

25 primarily a function of τ and a shortwave-infrared (SWIR) channel in which clouds are absorbing and the reflectance is primarily a function of r_e. Methods utilizing this principle are currently applied to all sensors with an appropriate combination of channels.

Despite the continuous advancements in both satellite sensors and retrieval algorithms, challenging issues remain. One of

30 them is the biases reported in liquid cloud optical and microphysical properties, associated with specific illumination conditions. These conditions include the backscattering directions, where the cloud glory effect is manifested, and scattering angles close to 140°, where the cloud bow effect, which is the equivalent of the rainbow created by cloud droplets, appears (Können, 2017). Retrieval failures and biases in τ and r_e have been reported for cloud glory and cloud bow in MODIS (Cho et al., 2015) and cloud bow in MODIS and the Multi-angle Imaging Spectroradiometer (MISR, Liang et al., 2015), while

angular biases under the same conditions were also found in retrievals from Polarization and Directionality of the Earth's Reflectances (POLDER) observations (Zeng et al., 2012).

Another issue in cloud optical properties retrieval, which relates to the cloud glory effect, is the width of the cloud droplet

5 size distribution assumed in the retrieval process. This width is usually represented by the effective variance (v_e) of the size distribution or other equivalent measures, e.g. the shape parameter μ (Petty and Huang, 2011). In case of passive satellite sensors that measure total reflectance, v_e is not retrieved; a constant value is instead assumed and used for the retrieval of τ and r_e of all liquid clouds. Typical v_e values used in satellite-based retrievals lie between 0.10 and 0.15. The former is the value used in MODIS Collection 6, ISCCP-H (Rossow, 2017) and PATMOS-x (Walther and Heidinger, 2012), while in the

10 Cloud_cci data records v_e equals 0.11 (McGarragh et al., 2018). For the CLARA-A and CLAAS records v_e equal to 0.15 is assumed (Karlsson et al., 2013; Stengel et al., 2014; Karlsson et al., 2017; Benas et al., 2017). In MODIS Collection 5, a standard deviation of a lognormal size distribution equal to 0.35 was used (Liang et al., 2015), which corresponds to a v_e equal to 0.13 (Nakajima and King, 1990). Studies including in situ measurements, however, suggest a significantly wider range of v_e values, depending on cloud types, regions (marine or continental, see e.g. Miles et al., 2000) but also for the same

15 cloud type (Igel and Van den Heever, 2017). While under most retrieval circumstances the sensitivity of τ and r_e to v_e is low, this is not the case for special illumination geometries, as was shown e.g. in Mayer et al. (2015) for the cloud glory conditions.

In the present study we analyze irregularities in the diurnal evolution of retrieved cloud optical and microphysical properties

20 (τ and r_e), appearing near the cloud glory and cloud bow geometries, and their sensitivity to the width of the assumed cloud droplet size distribution. For the analysis of the diurnal variability of optical properties, we use data from SEVIRI on board geostationary satellites Meteosat-8 and -10, and the Cloud Physical Properties (CPP) retrieval algorithm (Benas et al., 2017; Roebeling et al., 2006), used in the production of CLARA-A2 and CLAAS-2 data records. We focus primarily on a region over the southeast Atlantic and one characteristic day. This region is scanned by the two SEVIRI sensors of both Meteosat

25 satellites under different illumination conditions, so that possible effects near the cloud glory and near the cloud bow occur in the two retrievals at different times. While in principle the retrieval algorithm should compensate for the different viewing and illumination geometries, and the two products should agree under any circumstances, we show that this is not the case by monitoring the diurnal evolution of the retrieved optical properties.

30 The sensitivity of these effects to the width of the assumed size distribution is analyzed by performing retrievals using different values of the corresponding v_e. Intercomparisons of the products derived from these retrievals help in the assessment of their sensitivity and highlight the importance of selecting the appropriate value of v_e. Apart from this analysis, three additional retrievals are performed; one over the same region, but using a different spectral combination of visible and SWIR channels, and two over a land area of southern Africa, using both spectral combinations. Corresponding comparisons

of different underlying surfaces (ocean/land) and different channel retrievals provide further insights on the relative importance of these factors in the retrieval process.

In the following section we describe the two Meteosat satellites and the CPP retrieval algorithm in more detail, along with

5   the data used and the way these were processed. Section 3 includes the results, focusing first on the retrieval algorithm input and output over the South Atlantic region, their characteristics due to different illumination conditions (Sect. 3.1) and their dependence on the width of the assumed size distribution (Sect. 3.2). Comparisons between retrievals from different spectral pairs and over different underlying surfaces are presented in Sects. 3.3 and 3.4, followed by the discussion and conclusions.

2 Data and methodology

10   ### 2.1 Satellites

EUMETSAT operates four Meteosat Second Generation (MSG) satellites, namely Meteosat-8, -9, -10 and -11 (also referred to as MSG-1, -2, -3 and -4, respectively). All four are positioned in geostationary orbit, about 35786 km above the equator. In September 2016 MSG-1 was nominally positioned at 41.5° E longitude, covering mainly Africa and the Indian ocean, and in early 2017 the Indian Ocean Data Coverage (IODC) service became operational. MSG-3 was the primary operational

15   satellite for Africa, Europe and the Atlantic Ocean, nominally positioned at 0° longitude, between January 2013 and February 2018. The areas covered by MSG-1 and MSG-3 have a large overlap (see Fig. 1), comprising Africa, Europe, the Middle East and large oceanic regions, which offers new opportunities for synergistic usage of data from the two satellites.

It should be noted that the two satellites deviate from their nominal positions on a diurnal basis. In the period considered in

20   this study (March 2017), this deviation is most pronounced in the latitude of MSG-1, which ranges between approximately 5° S and 5° N on a 24-hour basis. This deviation alters the viewing geometry and estimated scattering angles, thus also affecting the retrieved optical properties. To avoid possible consequent misinterpretations, information on the exact position of each satellite, available on a 15-minute time slot basis, was included in the retrieval process.
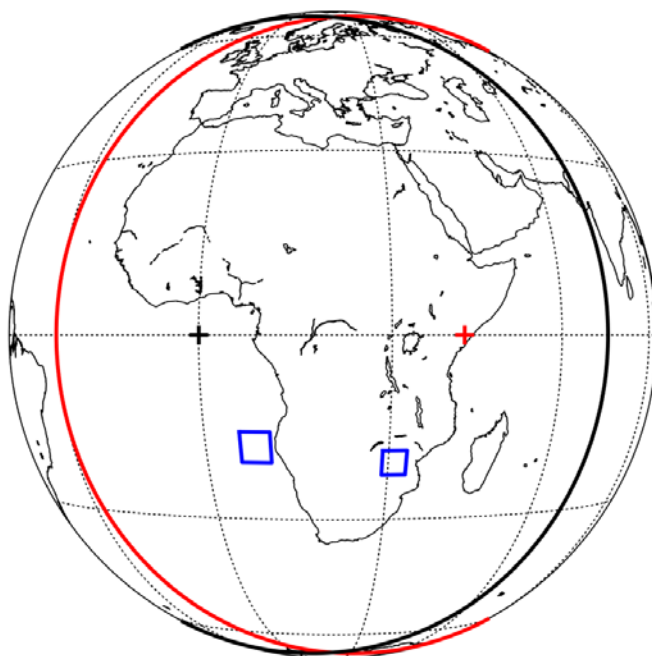
Figure 1: The overlap area created by the disks of MSG-1 (red line) and MSG-3 (black line). The red and black crosses show the corresponding nominal sub-satellite points. The blue rectangles show the primary study region west of the African coast (15°-20° S, 6°-11° E) and the secondary in the southern parts of Zimbabwe and Mozambique (18°-22° S, 29°-33° E).

SEVIRI is one of the main instruments on board the MSG satellites. It observes the Earth in 12 spectral channels between the visible and thermal infrared, acquiring measurements every 15 minutes at 3 km nadir resolution. The CPP algorithm uses measurements from one visible and one SWIR channel to retrieve τ and r_e. For SEVIRI, this is achieved by combining the channel near wavelength $\lambda = 0.6$ μm with either the 1.6 μm or the 3.9 μm channel (CM SAF, 2016). To ensure a valid

10 intercomparison between MSG-1 and MSG-3 reflectances and retrievals, calibration of SEVIRI shortwave channels on both satellites was performed using Aqua MODIS Collection 6 reflectances as a reference, instead of the operational EUMETSAT calibration. The approach is described in Meirink et al. (2013) and was extended in this study to include 2017. This yielded calibration slopes of 0.0267, 0.0229, 0.0235, and 0.0229 mW m^{-2} sr^{-1} (cm^{-1})$^{-1}$ for the MSG-1 0.6 μm, MSG-1 1.6 μm, MSG-3 0.6 μm, and MSG-3 1.6 μm channels, respectively.

15 **2.2 Retrieval Method**

The CPP algorithm requires a cloud mask, and several cloud top properties as input. The cloud mask as well as cloud top height and temperature are obtained using the Satellite Application Facility for Nowcasting (NWC SAF) GEOv2016

software package (NWC SAF, 2016; Derrien and Le Gléau, 2005). The cloud top phase retrieval is based on a modified version of the Pavolonis et al. (2005) algorithm, as described in Benas et al. (2017). In this study only liquid phase clouds are considered. The physical principle of the CPP approach was described in Nakajima and King (1990) and is presently used for the retrieval of cloud optical and microphysical properties from various satellite imagers. It relies on the dependence of

5   the cloud reflectance in a visible (non-absorbing) channel mainly on τ, and that in a SWIR (absorbing) channel on r_e. These different characteristics render possible the simultaneous retrieval of τ and r_e by comparison with simulated cloud reflectances in the visible and SWIR under different illumination conditions.

For the radiative transfer calculations, a two-parameter gamma size distribution of liquid cloud droplets is assumed, given in
10   Hansen (1971) and also described in Petty and Huang (2011):

$$n(r) = N_0 r^{\frac{1-3v_e}{v_e}} \exp\left(\frac{-r}{r_e v_e}\right)$$
(1)

The constant N_0 is provided in Hansen (1971) but is not required here, since the retrieval algorithm is based on normalized quantities. Mie scattering calculations are performed using a Mie code (De Rooij and Van der Stap, 1984), whereby the scattering matrix is calculated and provided in terms of generalized spherical functions. This output is then used as input for

15   the multiple scattering calculations based on the Doubling-Adding KNMI (DAK) radiative transfer model (De Haan et al., 1987; Stammes, 2001), for the simulation of top-of-atmosphere (TOA) reflectances of clouds in a Rayleigh atmosphere for different channels, which are stored in a lookup table (LUT; see below for its layout). The reflectances R are defined as:

$$R = \frac{\pi I}{E_0 \cos \theta_0}$$
(2)

where I is the radiance measured by the satellite in a specific channel, E_0 is the downwelling solar irradiance at TOA
20   contained within the channel's spectral response function and θ_0 is the solar zenith angle. Using radiative transfer calculations for three values of the surface albedo, the reflectances can be calculated for the actual surface albedo, which is assumed to be constant over ocean (0.05 in the 0.6 and 1.6 μm channels, and 0.02 in the 3.9 μm channel) and obtained from MODIS-based climatologies over land (Greuell et al. (2013) at 0.6 and 1.6 μm and Seemann et al. (2008) at 3.9 μm). The measured reflectances are corrected for absorption by atmospheric gases, of which concentrations are obtained from the

25   European Centre for Medium Range Weather Forecasting (ECMWF) Integrated Forecasting System (IFS) model (water vapour and ozone) or from climatologies (other trace gases). In case of the 3.9 μm channel, the measurement is further corrected for a contribution of thermal emission based on the IFS surface temperature and the retrieved cloud top temperature. A match between the measurements and the LUT of simulated reflectances is then sought, yielding the cloud optical properties τ and r_e.

30

To assess the sensitivity of the optical properties retrieval to the width of the liquid droplets size distribution, multiple Mie and DAK runs were performed, for the creation of seven LUTs. Each LUT corresponds to a different size distribution width,

represented by a different value of v_e. The seven values of v_e were selected following the approach of Arduini et al. (2005) and their typical reported range (0.01-0.30, see also Miles et al., 2000; Igel and Van den Heever, 2017). Figure 2 shows the corresponding seven size distributions for the visible wavelength (0.6 µm) and r_e = 12 µm (Fig. 2a) along with the scattering phase functions resulting from the Mie calculations (Fig. 2b). Cloud bow and glory features are apparent in all phase functions, along with differences in their shapes especially near the cloudbow and in the backscattering directions. Each LUT contains simulated reflectances at the required wavelengths for various values and ranges of θ_0, the viewing zenith angle (θ), the relative azimuth angle ($\Delta\phi = 180 - |\phi-\phi_0|$), τ and r_e. Table 1 summarizes these LUT characteristics.
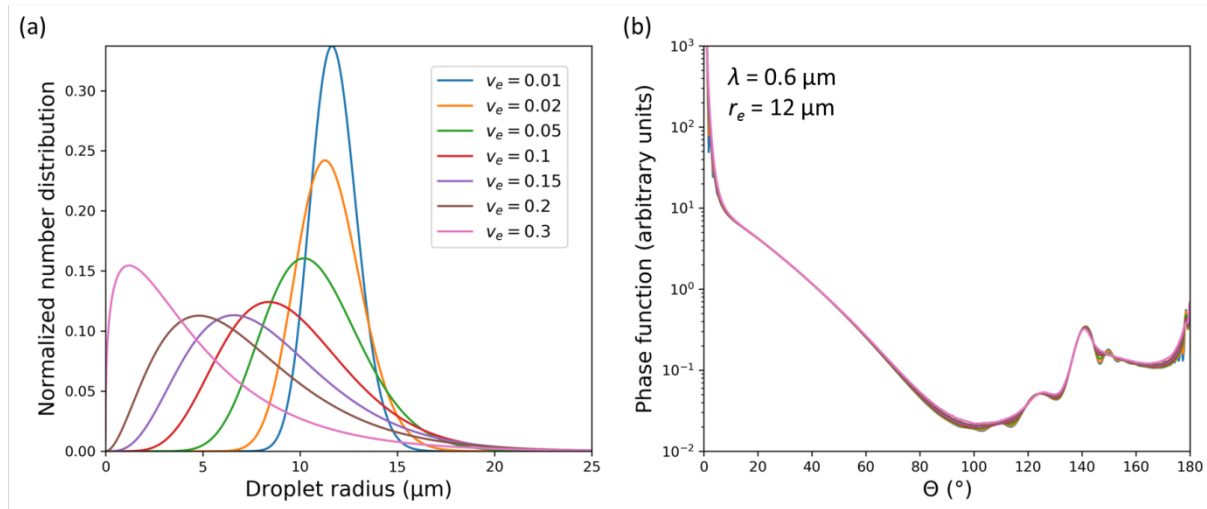
Figure 2: Normalized droplet size distributions for λ = 0.6 µm and r_e = 12 µm, for the seven values of effective variance v_e used in the Mie and DAK calculations (a), and corresponding scattering phase functions derived from Mie calculations (b).

Table 1. Values and numbers of points of the variables comprising the five dimensions of the cloud reflectance LUTs. Each value of effective variance (v_e, last row) corresponds to a different LUT.

Variable	Values	Number of points
$\cos(\theta_0)$	0.099-1 (θ_0: 0-84.3°)	73, Gauss-Legendre points
$\cos(\theta)$	0.099-1 (θ: 0-84.3°)	73, Gauss-Legendre points
$\Delta\phi$	0-180°	91, equidistant
τ	0 and 0.25-256	22, equidistant in $\log(\tau)$
r_e	3-34 µm	8, equidistant in $\log(r_e)$
v_e	0.01, 0.02, 0.05, 0.10, 0.15, 0.20, 0.30	7

2.3 Selection of study areas and days

Using the different LUTs, liquid cloud τ and r_e were retrieved from MSG-1 and MSG-3 for two selected days and regions. Specifically, days near the equinox were chosen so that the sun passed over the satellite, yielding glory viewing conditions. Subsequently, two study regions (one over ocean and one over land, see Fig. 1) were selected based on their high degree of

5 liquid cloud deck uniformity during specific days in 2017. For the oceanic region the CPP retrieval was performed for March 7, 2017, while for the land region the day selected was March 20, 2017. The CPP retrievals were performed separately for the pairs of channels 0.6 μm - 1.6 μm and 0.6 μm - 3.9 μm. Figure 3 shows the spatial coverage of the two areas with liquid clouds during the days selected. Based on the different viewing conditions, and the fact that larger viewing angles lead to larger cloud fractions retrieved, MSG-3 should yield more clouds over the continental region and less over the marine (see

10 also Fig. 1). The counterintuitive results in the latter case should be attributed to more ice clouds detected by MSG-1. While the reason for this difference is not obvious, the sizes of the two areas (5°×5° and 4°×4°) and their high spatial coverage with liquid clouds throughout these days, ensure the calculation of meaningful statistics of the retrieved cloud properties. In fact, liquid clouds cover more than 80% of these areas during the days selected, and especially in the cloud bow and glory time slots.
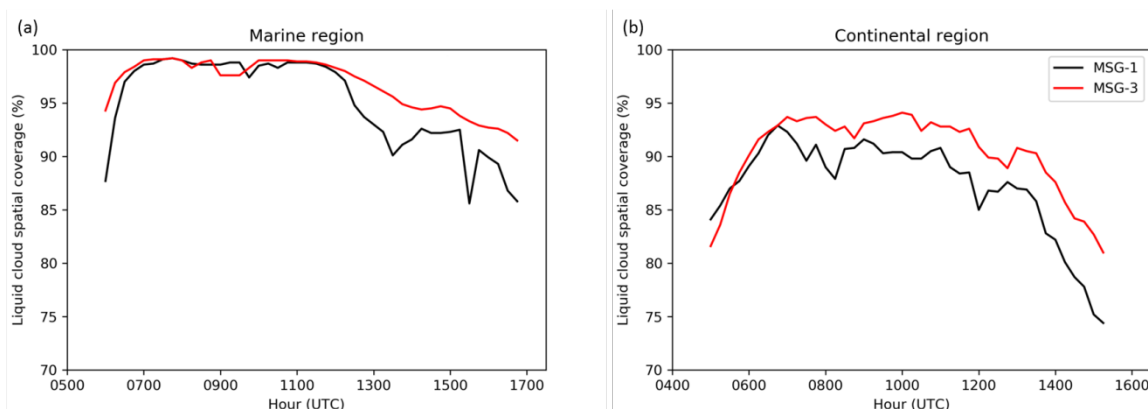
Figure 3: Spatial coverage (%) of the marine (a) and continental (b) regions with liquid clouds during March 7, 2017 and March 20, 2017, respectively, estimated separately from MSG-1 (black lines) and MSG-3 (red lines). The regions are indicated in Fig. 1.

20 Furthermore, although some afternoon time slots in MSG-1 could possibly be affected by sunglint conditions over the southeastern Atlantic, the good agreement between the two satellites during these time slots ensures that possible sunglint effects do not interfere with the results.

3 Results

3.1 Irregularities in the CPP diurnal cycle

Figure 4 shows the spatially averaged reflectances of the 0.6 μm and 1.6 μm channels used as input to the CPP algorithm over the southeast Atlantic on March 7, 2017, separately from MSG-1 and MSG-3. The corresponding CPP output, comprising τ and r_e, is also shown. Scattering angles from the two satellites during this day are shown in Figs. 4a and 4b,

5 along with dotted and dashed vertical lines which highlight the cloud glory and cloud bow geometries (maximum values and 140° scattering angles, respectively). Scattering angles (Θ) are computed from θ_0, θ and $\Delta\varphi$ based on:

$$\Theta = \cos^{-1}(\sin\theta_0 \sin\theta \cos\Delta\varphi - \cos\theta_0 \cos\theta) \tag{3}$$
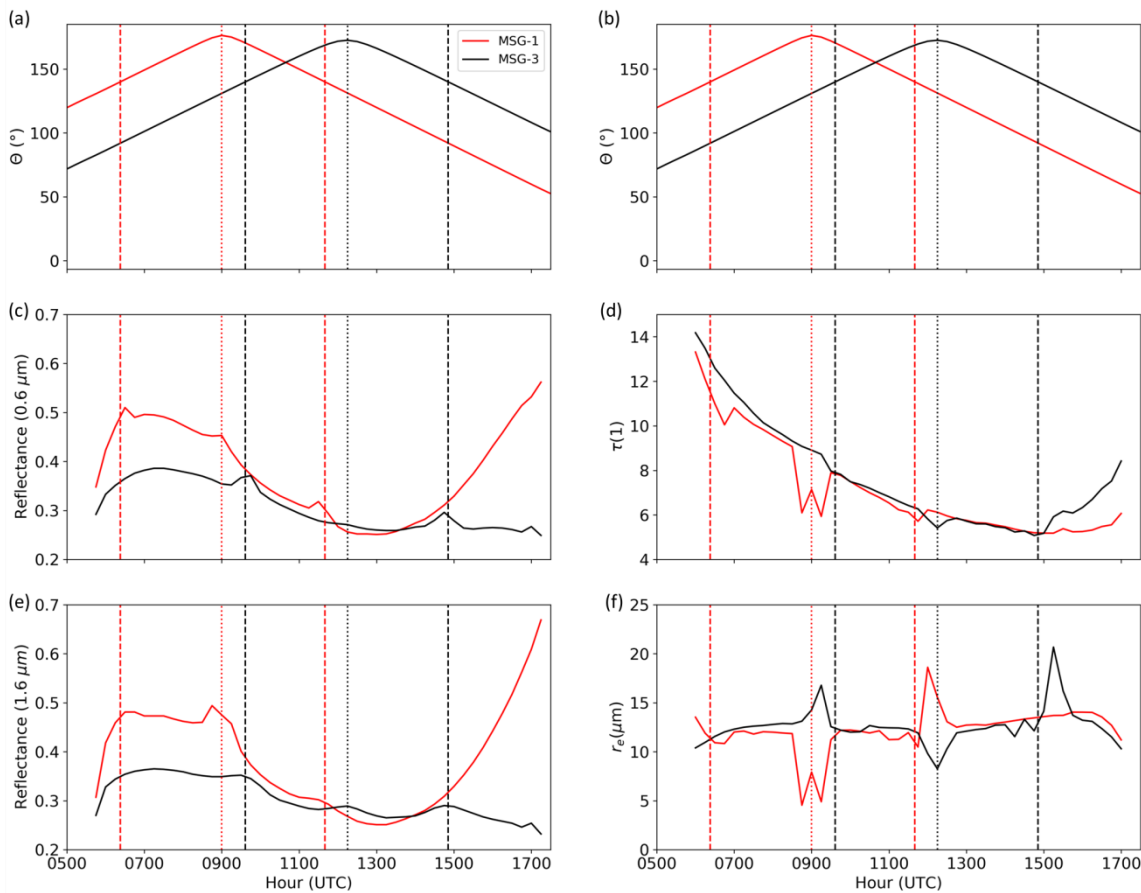
10 **Figure 4: Diurnal evolution of average cloudy-sky reflectances observed from SEVIRI at 0.6 μm (c) and 1.6 μm (e) and CPP output τ (d) and r_e (f) over the southeast Atlantic region on March 7, 2017. Scattering angles (a, b) are shown twice for visualization purposes. All data are shown separately for MSG-1 (red lines) and MSG-3 (black lines). The CPP output is based on retrievals with v_e = 0.15. Dotted vertical lines correspond to the maximum scattering angles, highlighting the cloud glory region, while dashed vertical lines are drawn at 140° scattering angles, roughly the cloud bow regions.**

It should be noted that the exact cloud bow angle varies with particle size. Nevertheless, it always lies around 140° (see also Fig. 2b), hence this angle was chosen here for visualization purposes. Both cloud glory and cloud bow are apparent as irregularities in the diurnal evolution of reflectances, especially in the visible channel, whereas their effect is partially smoothed in the SWIR. The cloud glory irregularity appears around the maximum scattering angle for that day and region,

5   which is 172°. Cloud bow irregularities, on the other hand, occur in scattering angles close to 142°. Large discrepancies between MSG-1 and MSG-3 reflectances appear late in the afternoon, with values increasing rapidly for low scattering angles.

Despite the possible differences in reflectances measured from the two sensors over the same area and time slot, which

10   should be attributed to the different illumination conditions, the retrieval algorithm should in principle compensate for these and ideally produce the same results, which correspond to the real conditions examined from two different angles. In practice, however, this is hardly ever achieved. Figures 4d and 4f show the retrieved τ and r_e separately from MSG-1 and MSG-3. These retrievals were based on $v_e = 0.15$, which is the value used in the CLAAS-2 CPP version. For both satellites, apparent irregularities are centered on the cloud glory in both τ and r_e, with most pronounced discrepancies for r_e. It appears,

15   however, that in the cloud bow time slots retrievals are rather normal, with big differences occurring in r_e for smaller scattering angles, namely close to 132°.
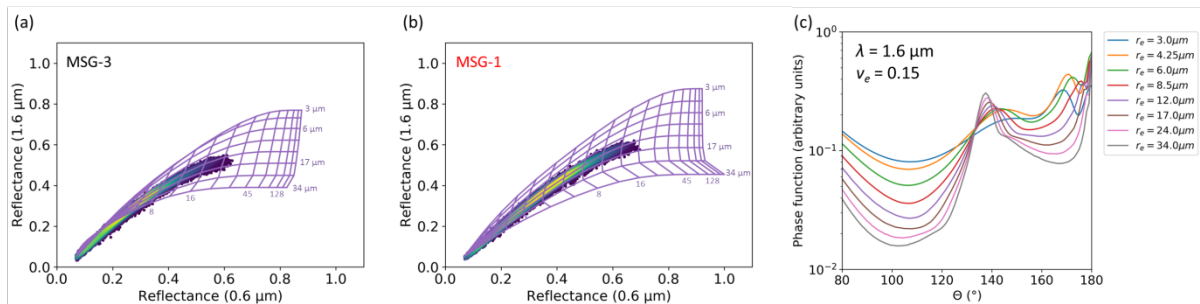
Figure 5: Plots of (atmospheric absorption corrected) reflectance observations from cloudy pixels and corresponding retrieval
20   **LUTs for the 15:15 UTC time slot in March 7, 2017 over the southeast Atlantic, separately for MSG-3 (a) and MSG-1 (b). (c)**
Phase functions at 1.6 µm wavelength used in the radiative transfer calculations for the eight r_e values of the LUTs, assuming v_e =
0.15.

Further analysis showed that these features are caused by a large number of observations falling outside the LUT,

25   specifically below, leading to r_e retrievals at its highest value (34 µm). This is illustrated in Fig. 5a, which shows the scatter plot of cloud reflectances observed from MSG-3 at 0.6 µm and 1.6 µm at 15:15 UTC, when r_e peaks (see Fig. 4f), overplotted with the LUT for the same illumination conditions, which was used in the retrieval. For comparison purposes, the same plot is shown for MSG-1 during the same time slot (Fig. 5b). It is apparent that the LUT now covers the

observations more adequately, leading to more reasonable r_e retrievals compared to adjacent time slots. The origin of this LUT inadequacy, occurring for scattering angles around 132°, can be traced back to the scattering phase functions used for the LUT calculations. Figure 5c shows the shape of these phase functions in the scattering angle range 80°-180° for all eight r_e values used in the LUT. The overlap of all the phase functions near 132° provides no information on the r_e, and leads to

5   the corresponding "collapse" in the left part of the LUT (Fig. 5a). A similar collapse occurs for scattering angles slightly larger than those of the cloud bow but their effect on the averaged retrievals is far less severe. On the other hand, scattering angles in the MSG-1 case lie around 86°, where Figs. 5b and 5c show that r_e is adequately retrievable. These characteristics in the phase functions were also reported for similar scattering angles in the case of MODIS where failure rates also increased (Cho et al., 2015). It should be noted, however, that this inadequacy is characteristic of optically thin clouds only.

10   It is obvious from the LUT shape in Fig. 5a that for clouds with higher τ, where multiple scattering prevails, r_e can be adequately retrieved.

3.2 Dependence of retrievals on the size distribution width

A similar analysis in the broader backscattering range (170°-180°) shows that the cause of the irregularities occurring in the cloud glory is different. It is known, in fact, that the shape of the cloud glory depends on r_e and the width of the droplet size

15   distribution, rather than τ (see e.g. Mayer et al., 2004). Figure 6 shows how the phase function changes in the backscattering range with varying r_e and v_e. Figure 6a constitutes a zoom-in of Fig. 5c. It shows that the distance of the characteristic cloud glory rings, appearing here as local maxima, from the 180° scattering angle, depends on the value of r_e for a given v_e. On the other hand, when r_e is given, the width of the size distribution controls the range of these maxima. This is depicted in Fig. 6b for a typical value of $r_e = 12$ μm and v_e ranging between 0.01 and 0.30. It is apparent that for narrow size distributions the

20   cloud glory is enhanced.
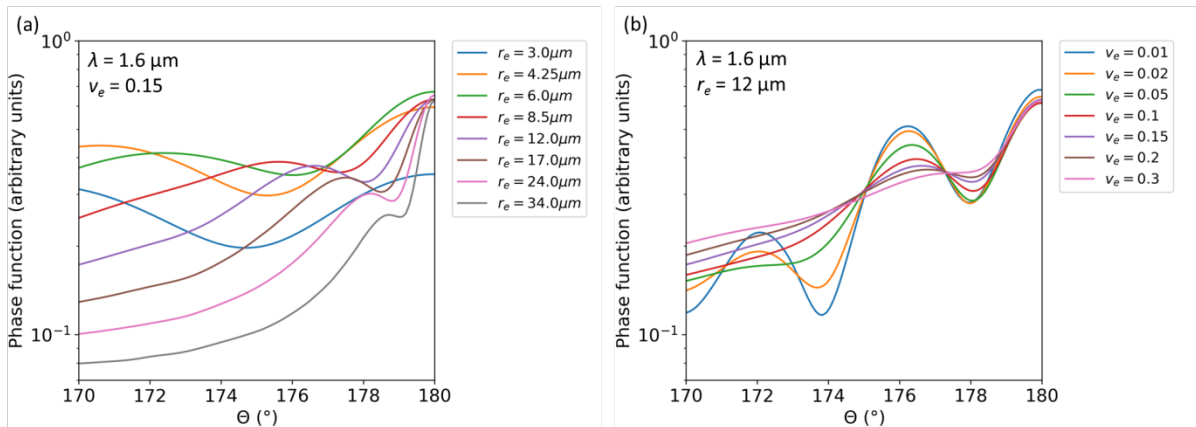
Figure 6: Dependence of the scattering phase function on r_e and v_e in the backscattering directions. (a) Phase functions at 1.6 µm wavelength used in the radiative transfer calculations for the eight r_e values of the LUTs, assuming v_e = 0.15. (b) Phase functions at 1.6 µm wavelength used in the radiative transfer calculations for the seven v_e values of the LUTs, assuming r_e = 12 µm.

5   Based on the previous analysis, it is natural to examine the CPP output under different assumptions regarding the width of the size distribution and the corresponding value of v_e. Figure 7 shows the differences between MSG-3 and MSG-1 τ and r_e retrievals for the seven v_e values examined. In the case of τ deviations occur only around the glory of each satellite, with the diurnal variation appearing smoother for narrower size distributions. These results show that the retrieval of τ is generally insensitive to the width of the size distribution, except for the cloud glory region. In the case of r_e however, large

10   irregularities appear in both the glory and near the cloud bow regions (see Fig. 4f), and their sensitivity to v_e is difficult to infer based on their differences (Fig. 7b). This is due to the distance between the two satellites and the angular distance between cloud bow and glory, which are similar, close to 40°. Hence, the retrievals from the two satellites are re-examined separately, as shown in Fig. 8.
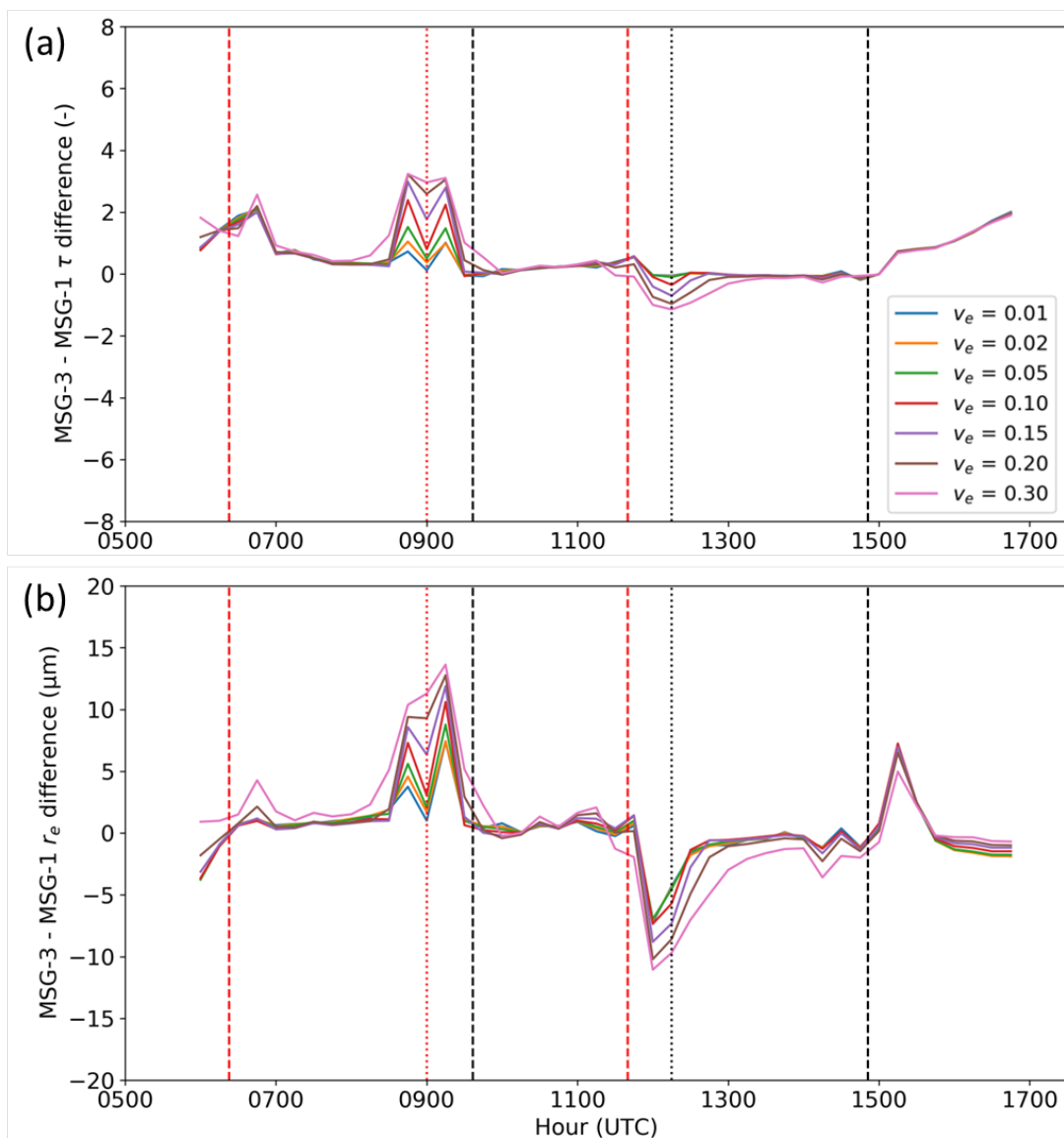
Figure 7: Differences between MSG-3 and MSG-1 retrievals of τ (a) and r_e (b) for the seven values of v_e examined, on March 7, 2017, over the southeast Atlantic. The vertical lines represent cloud glory (dotted) and cloud bow (dashed) geometries for MSG-1 (red) and MSG-3 (black), as in Figure 2.
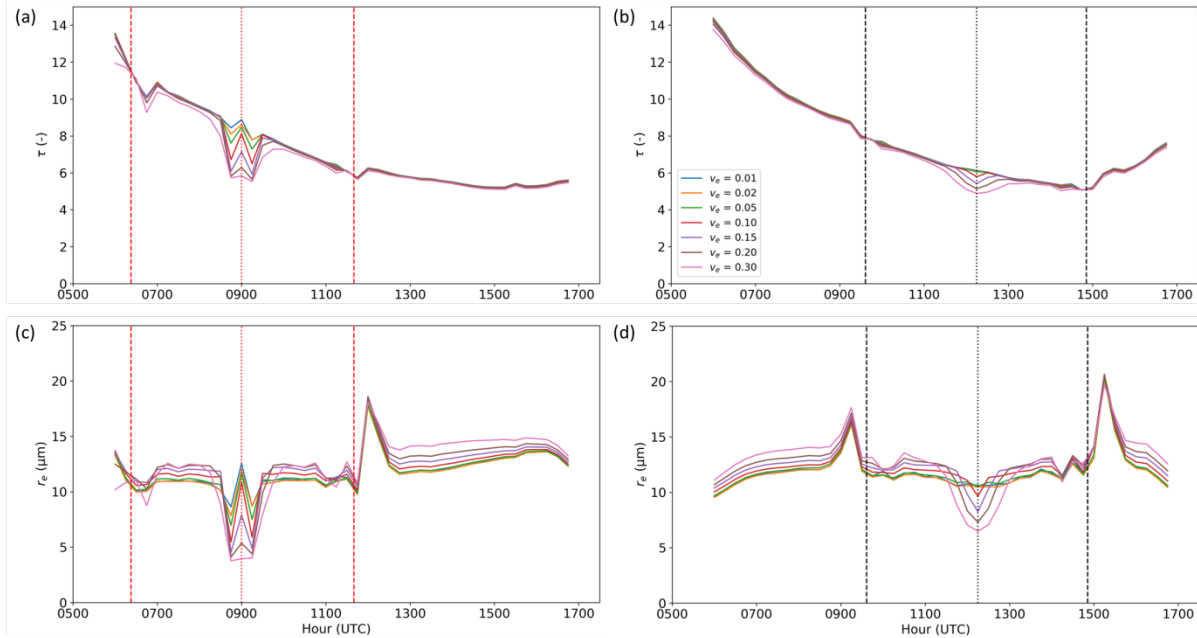
Figure 8: CPP retrievals of τ (a, b) and r_e (c, d) based on the 0.6 μm - 1.6 μm channel combination separately for MSG-1 (a, c) and MSG-3 (b, d), for the seven values of v_e examined, on March 7, 2017, over the southeast Atlantic. The seven v_e values are shown in (b). The vertical lines represent cloud glory (dotted) and cloud bow (dashed) geometries for MSG-1 (red) and MSG-3 (black), as in

5 **Figure 2.**

It is clear from Fig. 8 that v_e has a significant effect on r_e throughout the day, with differences occurring even during "normal" time slots. The effect on the glory is similar to the τ case, with larger irregularities for wider size distributions. In the 132° region, however, there is no sensitivity to the size distribution width. This is because the phase function

10 overlapping, shown in Fig. 5c, occurs for all values of v_e used.

Based on the irregularities near the cloud glory shown in Fig. 8 and the logical expectation that τ and r_e will exhibit a smooth diurnal variation, it appears that narrow droplet size distributions provide more natural outputs. This is confirmed by examining the number of pixels which are flagged during the retrieval process. Among others, CPP provides flags for pixels

15 where the pair of reflectances lies either above or below the LUT. Figure 9 shows the percent number of these pixels in the study region separately for MSG-1 and MSG-3 and for flags above and below the LUT.
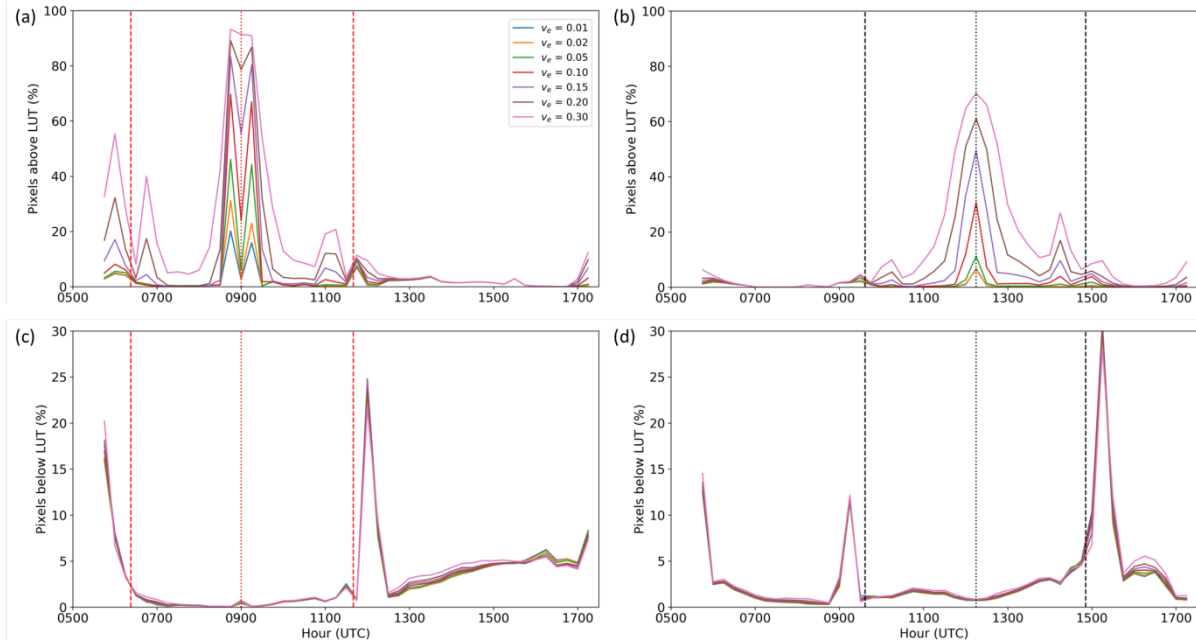
Figure 9: Fraction of flagged pixels (in %) with pairs of reflectances lying above (a, b) or below (c, d) the retrieval LUT, separately for MSG-1 (a, c) and MSG-3 (b, d) on March 7, 2017 over the southeast Atlantic. The results are shown for seven LUTs, corresponding to the seven values of v_e shown in (a).

The number of flagged pixels above the LUT increase rapidly around the cloud glory for wide droplet size distributions, covering up to 60% and 80% of the study region when v_e is higher than 0.15. While it appears that the narrower the size distribution, the least retrieval failures, this does not necessarily mean that the actual droplet size distribution is so narrow. Distributions with larger widths will have relatively more small particles included (see Fig. 2a). For smaller particles the size

10 parameter ($2\pi r/\lambda$) decreases, moving away from the regime where geometric optics hold, hence these distributions cannot capture the cloud glory adequately. On the other hand, the "collapse" of the LUT which occurs around the cloud bow, due to the overlap of the phase functions, causes failures below the LUT, of the order of 20% (see also Fig. 5a).

3.3 Retrievals based on the 3.9 μm channel

CPP retrievals for the same day and region were repeated using the 0.6 μm - 3.9 μm channel combination, instead of the 0.6

15 μm - 1.6 μm. It is well known that retrievals at the former wavelength are more sensitive to the cloud top compared to the latter, at which the photons penetrate deeper into the cloud (Platnick, 2000). As a result, and because r_e varies vertically, corresponding retrievals are in principle different. Different failure patterns between the two spectral combinations have also been reported, with more successful retrievals for the larger wavelength, which is less prone to failures due to cloud inhomogeneity (Cho et al., 2015).
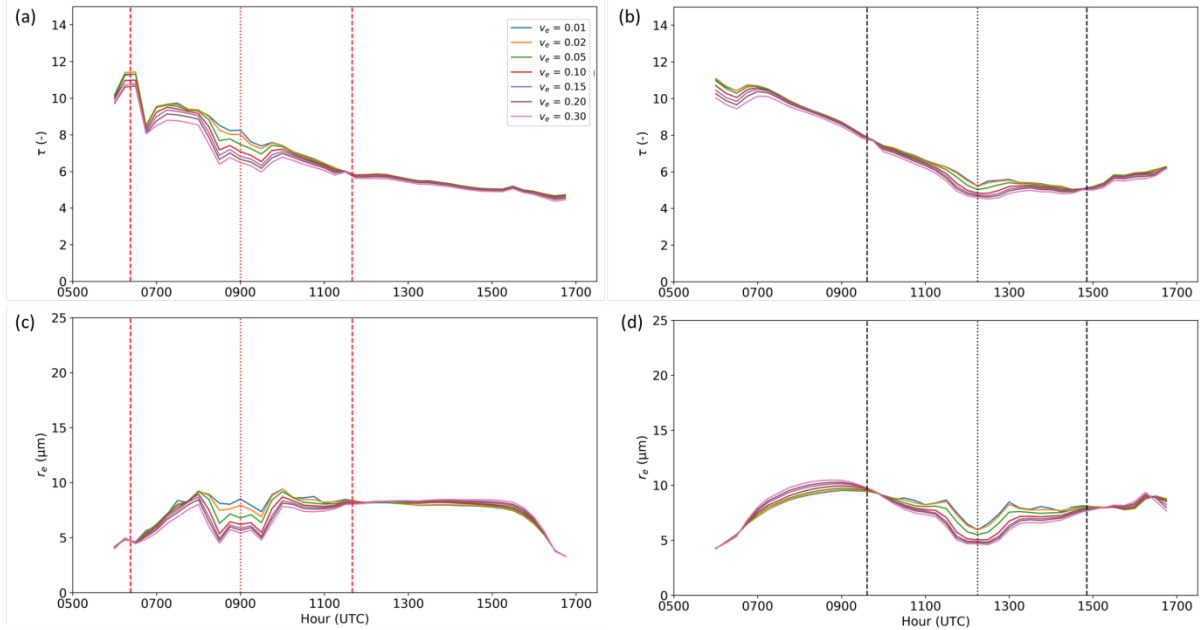
Figure 10: CPP retrievals of τ (a, b) and r_e (c, d) based on the 3.9 μm channel separately for MSG-1 (a, c) and MSG-3 (b, d), for the seven values of v_e examined, on March 7, 2017, over the southeast Atlantic. The seven v_e values are shown in (a). The vertical lines represent cloud glory (dotted) and cloud bow (dashed) geometries for MSG-1 (red) and MSG-3 (black), as in Figure 2.

Figure 10 shows the diurnal variation of τ and r_e retrieved using the 3.9 μm channel for the same day and region. Two prominent characteristics are directly distinguishable, compared to the corresponding 0.6 μm - 1.6 μm retrievals: a) a better discrimination of the diurnal patterns around the glory corresponding to $v_e < 0.10$ is possible, and b) there is no apparent irregularity near the cloud bow, which in the case of the 0.6 μm - 1.6 μm retrieval was caused by the phase functions overlap

10   at 132° scattering angle. The first characteristic suggests that in this specific combination of spectral channels and viewing geometry additional information is available regarding the width of the size distribution. In fact, for scattering angles close to 172°, which is the angle in the glory time slot for MSG-3 in this specific day and region, the single scattering phase functions that correspond to different size distribution widths are much more separated at the 3.9 μm wavelength (Fig. 11a) compared to the 1.6 μm (Fig. 6b). The second characteristic originates in a similar feature, namely non-overlapping scattering phase

15   functions of different r_e values in the 132° scattering angle region for the 3.9 μm wavelength (Fig. 11b) compared to the corresponding for the 1.6 μm (Fig. 5c). This feature stems from the fact that for larger wavelengths the cloud bow, which is a geometrical optics phenomenon, is less pronounced, and renders the 3.9 μm channel more suitable for the retrieval of more realistic diurnal variations of cloud optical properties. Less retrieval failures compared to the 0.6 μm - 1.6 μm retrieval were also found, similarly to the results reported by Cho et al. (2015) on corresponding MODIS channels, although they never

20   disappear completely from the cloud glory time slot. They rather range between 20% and 60%, depending on satellite and v_e. Near the cloud bow, however (132° scattering angle) they completely disappear.
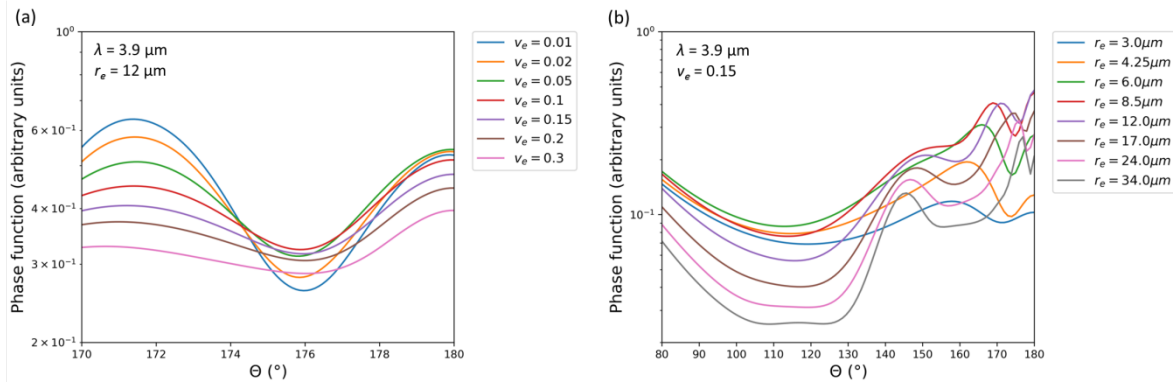
Figure 11: Dependence of the scattering phase functions at 3.9 µm wavelength on r_e and v_e in the backscattering directions. (a) Phase functions in the backscattering directions for the seven v_e values considered, assuming r_e = 12 µm. (b) Phase functions for the eight r_e values of the LUTs, assuming v_e = 0.15.

While a direct comparison of r_e values between the 0.6 µm - 1.6 µm and the 0.6 µm - 3.9 µm retrievals should be performed on a pixel basis, the overall smaller r_e values in the latter case hint to the presence of subpixel cloud heterogeneity (Zhang and Platnick, 2011). In fact, based on simulated MODIS retrievals, Bennartz and Rausch (2017) reported that for subpixel fractions of open water above 10% the retrieved r_e at 0.6 µm - 1.6 µm already starts to exceed the one retrieved at 0.6 µm - 3.9 µm. Apart from this, retrieval differences related to imperfect treatment of the 3.9 µm channel cannot be excluded, since this SEVIRI channel is rather broad and requires relatively large atmospheric correction.

3.4 Retrievals over the continental region

Part of the results presented so far are expected to apply for specific circumstances, namely an optically moderately thick marine Sc cloud over ocean. As previously explained, to examine possible differences caused by different cloud conditions, the same analysis was performed over a continental region, in the southern parts of Zimbabwe and Mozambique (18°-22° S, 29°-33° E, see also Fig. 1). The selection requirements here were also a spatial coverage of at least 80% with liquid clouds only, persistent in most time slots within a day. March 20, 2017 was selected, which is close to March 7, used in the marine case. Combined with the similar latitudes of the two regions, this ensures the presence of similar cloud glory and cloud bow conditions.

Retrievals based on the 0.6 µm - 1.6 µm channels for different values of v_e are shown in Figure 12. Values of τ reveal an optically much thicker cloud compared to the marine Sc case, with typical values between 20 and 30, while r_e values are also almost double those of the former case. Lack of data in late afternoon is due to the liquid cloud fraction, which decreases below 80% in these time slots (see also Fig. 3b). The cloud bow irregularities, especially in the r_e, are less pronounced

compared to the marine region. This should be attributed to the continental cloud being optically thicker, which leads to higher reflectance values. Hence, the spectral pairs of cloudy pixels will lie in the more orthogonal area of the LUT (see also Fig. 5), avoiding the LUT "collapse", which will affect thinner clouds. A closer look into the glory area, especially in the τ case, shows that larger v_e values now provide the smoother diurnal variability. This is consistent with thick continental

5 clouds, for which wider size distributions are expected. These results, however, are not directly comparable with the marine Sc case: the glory here occurs at 177°-178° scattering angle for both satellites. Compared to the 172° and even the 176° of MSG-3 and MSG-1 in the marine case, respectively, scattering phase function characteristics at the 0.6 μm channel (not shown), where τ retrieval is sensitive, can already differ significantly. A similar argument holds for r_e retrieval and corresponding angle and phase function differences in the 1.6 μm channel (Fig. 6b).
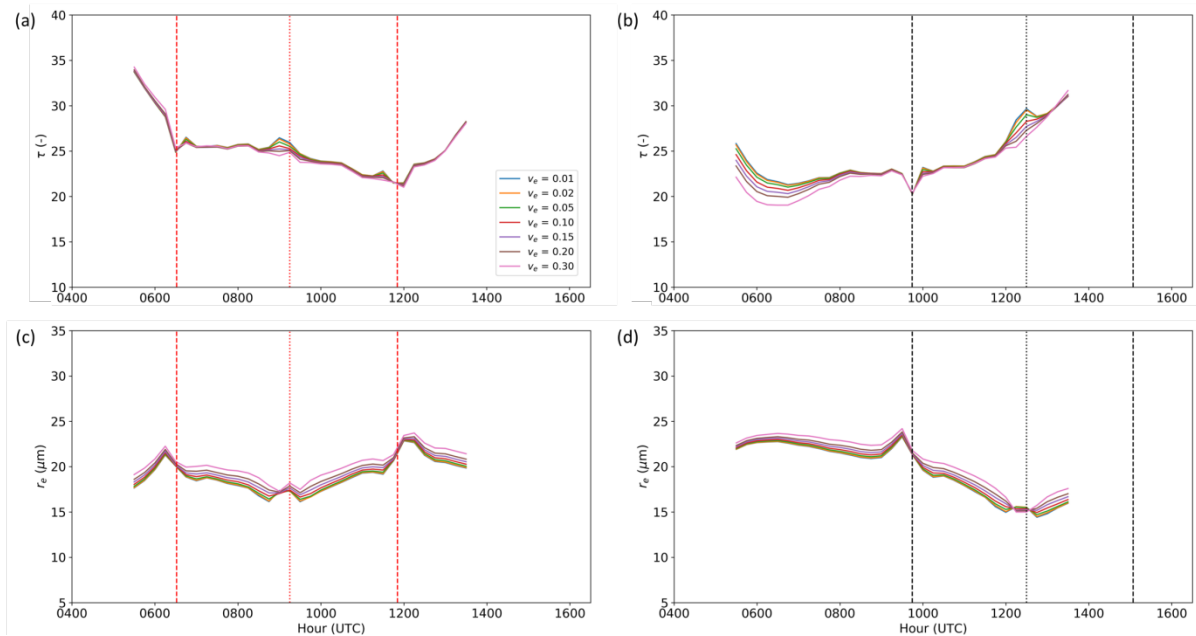
Figure 12: CPP retrievals of τ (a, b) and r_e (c, d) based on the 0.6 μm - 1.6 μm channel separately for MSG-1 (a, c) and MSG-3 (b, d), for the seven values of v_e examined, on March 20, 2017, over the continental region shown in Fig. 1. The vertical lines represent cloud glory (dotted) and cloud bow (dashed) geometries for MSG-1 (red) and MSG-3 (black), as in Fig. 2.

Figure 13 shows corresponding CPP output over the continental region using the 0.6 μm - 3.9 μm channels. As was also implied from the 0.6 μm - 1.6 μm retrievals over the same region (Fig. 12), wider distributions with v_e around 0.15 appear more realistic. The value of v_e also appears to affect the r_e retrieval throughout the day: higher v_e lead to higher r_e values, except near the glory region, where this pattern is reversed. The absence of any cloud bow feature, and the collapse of r_e

20 retrievals near the cloud glory can again be attributed to corresponding 3.9 μm phase function characteristics in these scattering angles (see also Figs. 11b and 11a respectively).
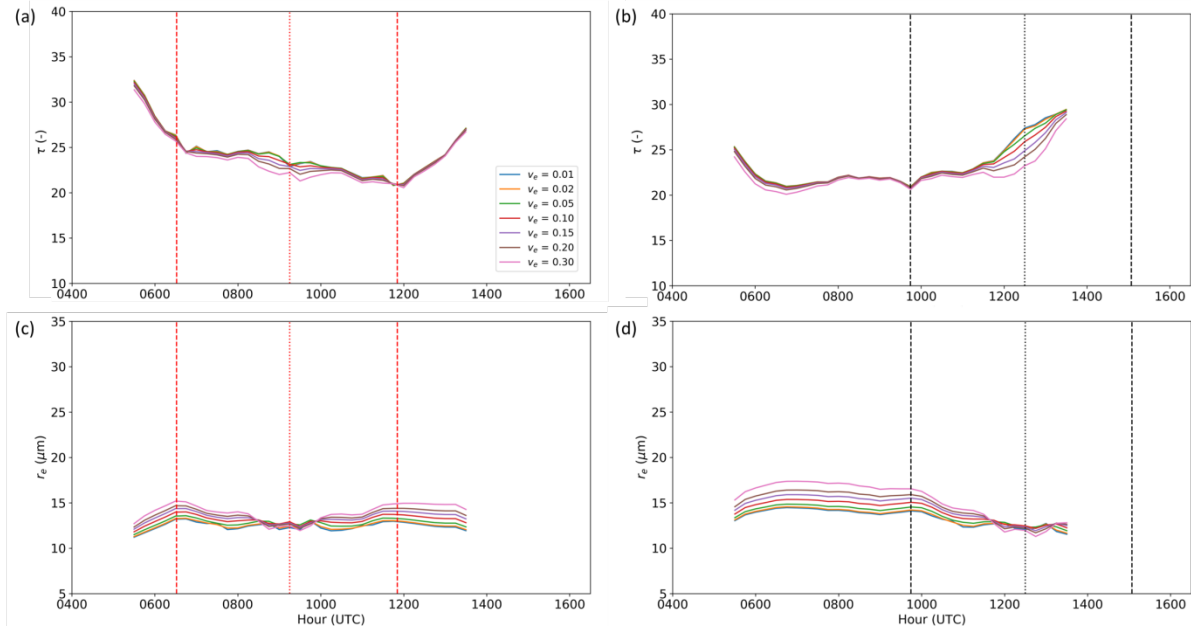
Figure 13: CPP retrievals of τ (a, b) and r_e (c, d) based on the 3.9 μm channel separately for MSG-1 (a, c) and MSG-3 (b, d), for the seven values of v_e examined, on March 20, 2017, over the continental region shown in Fig. 1. The vertical lines represent cloud glory (dotted) and cloud bow (dashed) geometries for MSG-1 (red) and MSG-3 (black), as in Fig. 2.

Regarding failure rates in the continental case, it is important noting that in the glory time slot they lie around 10%, never exceeding 20% in any channel combination and v_e value, while in the cloud bow they lie around 20% in the 0.6 μm - 1.6 μm retrieval and practically disappear in the 0.6 μm - 3.9 μm, similarly to the marine case. Since the maximum backscattering angles are quite different between the marine and the continental case, decreased flagged pixels in the latter case might be

10 due to this difference.

4 Discussion and Summary

In the present study irregularities in retrieved τ and r_e from satellite-based passive imagers were investigated using two MSG satellites. Taking advantage of the large overlap area between MSG-1 and MSG-3, a marine and a continental region were analyzed under different illumination and viewing conditions. Results showed that these irregularities are related to

15 scattering phase function characteristics near the cloud bow and cloud glory domains. In the latter case, retrievals were found to be sensitive to the width of the assumed droplet size distribution, expressed by v_e.

The analysis conducted here raises the question of the most appropriate value of v_e assumed in the retrieval. Measurements from many campaigns have been used for the estimation of the width of the droplet size distribution (see e.g. tables 1 and 2

in Miles et al., 2000 and table 1 in Igel and Van den Heever, 2017). If the corresponding width measures reported in these studies are converted to v_e, they lead to a range of values very similar to 0.01-0.30, as was used in Arduini et al. (2005) and in the present study. These results are not contradictory, since different size distribution widths are expected for different cloud types and under different conditions.

Table 2. Typical values and ranges of v_e found in observational studies and corresponding review papers.

Cloud type	v_e (±1σ)
Continental (Miles et al., 2000)	0.20 ± 0.17
Marine (Miles et al., 2000)	0.17 ± 0.15
Marine Sc (Miles et al., 2000)	0.13 ± 0.08
Marine Sc (Mayer et al., 2004)	0.01 ± 0.002
Marine Sc (Painemal & Zuidema, 2011)	0.07 ± 0.04 (average profile)
	0.04 ± 0.04 (cloud top)
Shallow Cu (Igel & van den Heever, 2017)	0.09 ± 0.04

Table 2 summarizes v_e values obtained from existing observational studies, where different measures of the width of the droplet size distribution were converted to v_e. The v_e values from Miles et al. (2000) and Igel & van den Heever (2017) were

10 based on their tables, in which results from various measurement campaigns are summarized. Wider droplet size distributions are generally found in continental clouds compared to marine ones. In marine only clouds, Sc decks exhibit even narrower distributions. A very narrow size distribution, corresponding to $v_e = 0.01$, was deduced from Mayer et al. (2004) based on aircraft measurement specifically in the cloud glory area, where information on the distribution width is available. Additionally, Painemal and Zuidema (2011), presenting results from a measurement campaign over the Southeast

15 Pacific Sc deck, report values of the "k" parameter, which is an equivalent measure of the size distribution width, varying with cloud height. Specifically, they estimate values of k equal to 0.8 and 0.88 for the average profile and the cloud-top respectively, which correspond to v_e equal to 0.07 and 0.04. More recently, Grosvenor et al. (2018) provided a useful discussion on the effect of the size distribution width on the estimation of CDNC and concluded that a value of 0.10 for v_e is likely to be an overestimation.

The conclusions drawn from the present study are similar, showing that the assumption of narrower distributions, with v_e around 0.05, leads to more reasonable retrievals, at least for the marine Sc cloud type. This is further emphasized by the results over the continental region (Sect. 3.4), where a wider size distribution appears more reasonable. These differences, along with the additional information provided by using different spectral pairs (Sect. 3.3), highlight the potential of passive

25 geostationary imagers to retrieve v_e under specific circumstances. The required information seems to be available in the cloud glory time slot, and future research will focus on the attempt to retrieve v_e from SEVIRI in regions with homogeneous liquid cloud cover under glory illumination conditions.

Acknowledgements

This work was performed within CM SAF funded by EUMETSAT.

References

Arduini, R. F., Minnis, P., Smith, W. L., Ayers, J. K., Khaiyer, K. K., and Heck, P.: Sensitivity of satellite-retrieved cloud
properties to the effective variance of cloud droplet size distribution, Proc. 15th ARM Science Team Meeting, 2005.

Benas, N., Finkensieper, S., Stengel, M., van Zadelhoff, G.-J., Hanschmann, T., Hollmann, R., and Meirink, J. F.: The MSG-
SEVIRI-based cloud property data record CLAAS-2, Earth Syst. Sci. Data, 9, 415-434, doi: 10.5194/essd-9-415-2017, 2017.
Bennartz, R. and Rausch, J.: Global and regional estimates of warm cloud droplet number concentration based on 13 years of
AQUA-MODIS observations, Atmos. Chem. Phys., 17, 9815-9836, doi: 10.5194/acp-17-9815-2017, 2017.

Cho, H. M., Zhang, Z., Meyer, K., Lebsock, M., Platnick, S., Ackerman, A. S., Di Girolamo, L., Labonnote, L., Cornet, C.,
Riedi, J., and Holz, R.: Frequency and causes of failed MODIS cloud property retrievals for liquid phase clouds over global
oceans, J. Geophys. Res.- Atmos., 120, 4132-4154, doi: 10.1002/2015JD023161, 2015.

CM SAF: Algorithm Theoretical Basis Document, SEVIRI Cloud Physical Products, CLAAS Edition 2, EUMET SAT
Satellite Application Facility on Climate Monitoring, SAF/CM/KNMI/ATBD/SEVIRI/CPP, Issue 2, Rev. 2, doi:
10.5676/EUM_SAF_CM/CLAAS/V002, 2016.

De Haan, J. F., Bosma, P., and Hovenier, J. W.: The adding method for multiple scattering calculations of polarized light,
Astron. Astrophys., 183, 371–391, 1987.

De Rooij, W. A. and Van der Stap, C. C. A. H.: Expansion of Mie scattering matrices in generalized spherical functions,
Astron. Astr., 131, 237–248, 1984.

Derrien, M. and Le Gléau, H.: MSG/SEVIRI cloud mask and type from SAFNWC, Int. J. Remote Sens., 26, 4707–4732,
2005.

Greuell, W., Meirink, J. F., and Wang, P.: Retrieval and validation of global, direct, and diffuse irradiance derived from
SEVIRI satellite observations, J. Geophys. Res., 118, 2340–2361, doi:10.1002/jgrd.5019, 2013.

Grosvenor, D. P., Sourdeval, O., Zuidema, P., Ackerman, A., Alexandrov, M. D., Bennartz, R., et al.: Remote sensing of droplet number concentration in warm clouds: A review of the current state of knowledge and perspectives, Rev. Geophys., 56. doi: 10.1029/2017RG000593, 2018.

5   Hansen, J.: Multiple scattering of polarized light in planetary atmospheres. Part II. Sunlight reflected by terrestrial water clouds, J. Atmos. Sci., 28, 1400–1426, 1971.

Heidinger, A. K., Foster, M. J., Walther, A., and Zhao, Z.: The Pathfinder Atmospheres Extended (PATMOS-x) AVHRR climate data set, B. Am. Meteorol. Soc., 95, 909–922, doi: 10.1175/BAMS-D-12-00246.1, 2014.

Igel, A. L., and S. C. van den Heever: The importance of the shape of cloud droplet size distributions in shallow cumulus clouds. Part I: Bin microphysics simulations, J. Atmos. Sci., 74, 249–258, doi: 10.1175/JAS-D-15-0382.1, 2017.

Karlsson, K.-G., Riihelä, A., Müller, R., Meirink, J. F., Sedlar, J., Stengel, M., Lockhoff, M., Trentmann, J., Kaspar, F.,
15   Hollmann, R., and Wolters, E.: CLARA-A1: a cloud, albedo, and radiation dataset from 28 yr of global AVHRR data, Atmos. Chem. Phys., 13, 5351–5367, doi:10.5194/acp-13-5351-2013, 2013.

Karlsson, K.-G., Anttila, K., Trentmann, J., Stengel, M., Meirink, J. F., Devasthale, A., Hanschmann, T., Kothe, S., Jääskeläinen, E., Sedlar, J., Benas, N., van Zadelhoff, G.-J., Schlundt, C., Stein, D., Finkensieper, S., Håkansson, N., and
20   Hollmann, R.: CLARA-A2: the second edition of the CM SAF cloud and radiation data record from 34 years of global AVHRR data, Atmos. Chem. Phys., 17, 5809-5828, doi: 10.5194/acp-17-5809-2017, 2017.

Können, G. P.: Rainbows, halos, coronas and glories. Beautiful sources of information, Bull. Amer. Meteor. Soc., 98, 485–494, doi: 10.1175/BAMS-D-16-0014.1, 2017.

Liang, L., Di Girolamo, L., and Sun, W.: Bias in MODIS cloud drop effective radius for oceanic water clouds as deduced from optical thickness variability across scattering angles, J. Geophys. Res.-Atmos., 120, 7661–7681, doi: 10.1002/2015JD023256, 2015.

30   Mayer, B., Schröder, M., Preusker, R., and Schüller, L.: Remote sensing of water cloud droplet size distributions using the backscatter glory: a case study, Atmos. Chem. Phys., 4, 1255-1263, doi: 10.5194/acp-4-1255-2004, 2004.

McGarragh, G. R., Poulsen, C. A., Thomas, G. E., Povey, A. C., Sus, O., Stapelberg, S., Schlundt, C., Proud, S., Christensen, M. W., Stengel, M., Hollmann, R., and Grainger, R. G.: The Community Cloud retrieval for CLimate (CC4CL) – Part 2: The optimal estimation approach, Atmos. Meas. Tech., 11, 3397-3431, doi: 10.5194/amt-11-3397-2018, 2018.

5 Meirink, J. F., Roebeling, R. A., and Stammes, P.: Inter-calibration of polar imager solar channels using SEVIRI, Atmos. Meas. Tech., 6, 2495-2508, doi: 10.5194/amt-6-2495-2013, 2013.

Miles, N. L., J. Verlinde, and E. E. Clothiaux: Cloud droplet size distributions in low-level stratiform clouds, J. Atmos. Sci., 57, 295–311, 2000.

Nakajima, T. and King, M. D.: Determination of the Optical Thickness and Effective Particle Radius of Clouds from Reflected Solar Radiation Measurements, Part 1: Theory, J. Atmos. Sci., 47, 1878–1893, 1990.

NWC SAF: Algorithm Theoretical Basis Document for the Cloud Product Processors of the NWC GEO, EUMETSAT
15 Satellite Application Facility on Nowcasting and Short range Forecasting, NWC/CDOP2/GEO/MFL/SCI/ATBD/Cloud, Issue 1, Rev. 1, 15 October 2016.

Painemal, D. and Zuidema, P.: Assessment of MODIS cloud effective radius and optical thickness retrievals over the Southeast Pacific with VOCALS-REx in situ measurements, J. Geophys. Res., 116, D24206, doi: 10.1029/2011jd016155,
20 2011.

Pavolonis, M. J., Heidinger, A. K., and Uttal, T.: Daytime global cloud typing from AVHRR and VIIRS: Algorithm description, validation, and comparison, J. Appl. Meteorol., 44, 804–826, doi: 10.1175/JAM2236.1, 2005.

25 Petty, G. W. and Huang, W.: The modified gamma size distribution applied to inhomogeneous and nonspherical particles: Key relationships and conversions, J. Atmos. Sci., 68, 1460–1473, doi: 10.1175/2011JAS3645.1, 2011.

Pincus, R., Platnick, S., Ackerman, S. A., Hemler, R. S., and Hofmann, R. J.: Reconciling simulated and observed views of clouds: MODIS, ISCCP, and the limits of instrument simulators, J. Clim., 25, 4699-4720, doi: 10.1175/JCLI-D-11-00267.1,
30 2012.

Platnick, S.: Vertical photon transport in cloud remote sensing problems, J. Geophys. Res., 105, 22 919–22 935, doi: 10.1029/2000JD900333, 2000.

Platnick, S., Meyer, K. G., King, M. D., Wind, G., Amarasinghe, N., Marchant, B., Arnold, G. T., Zhang, Z., Hubanks, P. A., Holz, R. E., Yang, P., Ridgway, W. L., and Riedi, J.: The MODIS cloud optical and microphysical products: Collection 6 updates and examples from Terra and Aqua, IEEE Trans. Geosci. Remote Sens., 55, 502–525, doi: 10.1109/TGRS.2016.2610522, 2017.

Roebeling, R. A., Feijt, A. J., and Stammes, P.: Cloud property retrievals for climate monitoring: implications of differences between SEVIRI on METEOSAT-8 and AVHRR on NOAA-17, J. Geophys. Res., 111, D20210, doi: 10.1029/2005JD006990, 2006.

10 Rossow, W. B.: Climate Data Record Program (CDRP): Climate Algorithm Theoretical Basis Document (C-ATBD) International Satellite Cloud Climatology Project (ISCCP) H-Series, CDRPATBD-0872, Asheville, North Carolina, USA, 179 pp., 2017.

Seemann, S.W., E. E. Borbas, R. O. Knuteson, G. R. Stephenson, H.-L. Huang: Development of a Global Infrared Land
15 Surface Emissivity Database for Application to Clear Sky Sounding Retrievals from Multi-spectral Satellite Radiance Measurements, J. Appl. Meteorol. Clim., 47, 108-123, 2008.

Stammes, P.: Spectral radiance modelling in the UV-Visible range, IRS 2000: Current problems in Atmospheric Radiation, edited by: Smith, W. L. and Timofeyev, Y. M., A. Deepak Publ., Hampton, VA, 385–388, 2001.

Stengel, M., Kniffka, A., Meirink, J. F., Lockhoff, M., Tan, J., and Hollmann, R.: CLAAS: the CM SAF cloud property data set using SEVIRI, Atmos. Chem. Phys., 14, 4297-4311, doi: 10.5194/acp-14-4297-2014, 2014.

Stengel, M., Stapelberg, S., Sus, O., Schlundt, C., Poulsen, C., Thomas, G., Christensen, M., Carbajal Henken, C., Preusker,
25 R., Fischer, J., Devasthale, A., Willén, U., Karlsson, K.-G., McGarragh, G. R., Proud, S., Povey, A. C., Grainger, R. G., Meirink, J. F., Feofilov, A., Bennartz, R., Bojanowski, J. S., and Hollmann, R.: Cloud property datasets retrieved from AVHRR, MODIS, AATSR and MERIS in the framework of the Cloud_cci project, Earth Syst. Sci. Data, 9, 881-904, doi: 10.5194/essd-9-881-2017, 2017.

30 Walther, A. and Heidinger, A. K.: Implementation of the Daytime Cloud Optical and Microphysical Properties Algorithm (DCOMP) in PATMOS-x, J. Appl. Meteorol. Clim., 51, 1371–1390, doi:10.1175/JAMC-D-11-0108.1, 2012.

Wood, R.: Stratocumulus clouds, Mon. Weather Rev., 140, 2373– 2423, doi: 10.1175/MWR-D-11-00121.1, 2012.

Wood, R. and Hartmann, D. L.: Spatial Variability of Liquid Water Path in Marine Low Cloud: The Importance of Mesoscale Cellular Convection, J. Clim., 19, 1748–1764, 2006.

Young, A. H., Knapp, K. R., Inamdar, A., Hankins, W., and Rossow, W. B.: The International Satellite Cloud Climatology
5   Project H-Series climate data record product, Earth Syst. Sci. Data, 10, 583-593, doi: 10.5194/essd-10-583-2018, 2018.

Zeng, S., Cornet, C., Parol, F., Riedi, J., and Thieuleux, F.: A better understanding of cloud optical thickness derived from the passive sensors MODIS/AQUA and POLDER/PARASOL in the A-Train constellation, Atmos. Chem. Phys., 12, 11245-11259, doi: 10.5194/acp-12-11245-2012, 2012.

Zhang, Z. and Platnick, S.: An assessment of differences between cloud effective particle radius retrievals for marine water clouds from three MODIS spectral bands, J. Geophys. Res.-Atmos., 116, D20215, doi:10.1029/2011JD016216, 2011.

Zhou, C., Zelinka, M. D., and Klein, S. A.: Impact of decadal cloud variations on the Earth's energy budget Nat. Geosci., 9,
15   871–874, doi: 10.1038/ngeo2828, 2016.